AIP | Physics of Plasmas

Properties of high-β microturbulence and the non-zonal transition

M. J. Pueschel, D. R. Hatch, T. Görler, W. M. Nevins, F. Jenko et al.

Citation: Phys. Plasmas **20**, 102301 (2013); doi: 10.1063/1.4823717
View online: http://dx.doi.org/10.1063/1.4823717
View Table of Contents: http://pop.aip.org/resource/1/PHPAEN/v20/i10
Published by the AIP Publishing LLC.

Properties of high-β microturbulence and the non-zonal transition

M. J. Pueschel,[1] D. R. Hatch,[2,3] T. Görler,[2] W. M. Nevins,[4] F. Jenko,[2] P. W. Terry,[1] and D. Told[2]
[1]*Department of Physics, University of Wisconsin-Madison, Madison, Wisconsin 53706, USA*
[2]*Max-Planck-Institut für Plasmaphysik, EURATOM Association, D-85748 Garching, Germany*
[3]*Institute for Fusion Studies, University of Texas at Austin, Austin, Texas 78712, USA*
[4]*Lawrence Livermore National Laboratory, Livermore, California 94551, USA*

(Received 16 April 2013; accepted 10 September 2013; published online 1 October 2013)

The physics underlying the non-zonal transition [M. J. Pueschel *et al.*, Phys. Rev. Lett. **110**, 155005 (2013)] are explored in detail, and various studies are presented which support the theory that critically weakened zonal flows are indeed responsible for the failure of ion-temperature-gradient-driven turbulence at high plasma β to saturate at typical transport values. Regarding flux-surface-breaking magnetic fluctuations and their impact on zonal flows, numerical approaches to obtaining zonal flow residuals are elaborated on, and simulation results are shown to agree with analytical predictions, corroborating the interpretation that flux-surface-breaking magnetic fluctuations cause the transition. Consistently, the zonal-flows-related energetics of the turbulence are found to change fundamentally when exceeding the threshold. © *2013 AIP Publishing LLC*.
[http://dx.doi.org/10.1063/1.4823717]

I. INTRODUCTION

Operational limits regarding the maximum plasma pressure achievable in fusion devices are an important field of study, both in light of plasma performance and the underlying physics. When attempting to heat an experiment beyond such thresholds, a large increase in the heat and particle transport results. One potential such limit is the non-zonal transition (NZT)[1]; while other pressure limits are associated with linear instabilities—of either fluid or kinetic nature—being excited at their respective thresholds, the NZT is a more complex, fundamentally nonlinear phenomenon. In addition to providing an encompassing explanation for the long-standing question why gyrokinetic codes see a sudden onset of extreme transport values well below the ballooning threshold for certain parameters, the concept of the NZT may also be applicable to actual fusion experiments.

The present paper aims to provide detailed background information on the results reported in Ref. 1, as well as shed more light on the physics underlying the NZT, in the process examining a variety of different physical effects. For convenience, the central properties of the NZT are summarized next.

Turbulent fluctuations of the magnetic potential $A_\parallel$ can be split into resonant and non-resonant components, meaning the extended ballooning structure[2] is symmetric or anti-symmetric, respectively (see Ref. 3 for more details). Typically, non-resonant potentials do not break magnetic flux surfaces since the radial displacement $\Delta r_{1/2}$ of a given field line—as it moves poloidally from the inboard to the outboard midplane—is canceled on its onward path, where the second half poloidal turn leads to a displacement $\Delta r_{2/2} \approx -\Delta r_{1/2}$. If, however, $\Delta r_{1/2}$ exceeds the radial correlation length λ_{Bxx} of the radial magnetic field $B_x = k_y A_\parallel$, with the binormal wavenumber k_y normalized to the ion sound gyroradius ρ_s, the second half turn starts to decorrelate from the first, and the field line will not return to its original radial position. As $\Delta r_{1/2}$ scales with the normalized electron pressure β, this results in the non-resonant component of $A_\parallel$ becoming flux-surface-breaking at a critical $\beta_{\mathrm{crit}}^{\mathrm{NZT}}$ and in a sudden increase of the magnetic stochasticity.[4] Zonal flows, in turn, are susceptible to such stochasticity as broken flux surfaces lead to radial currents, shorting out radial structures of the electrostatic potential. Therefore, ion temperature gradient (ITG) modes, which rely on zonal flows for saturation, can no longer saturate at typical levels of the heat flux and instead will continue to grow after some transient saturation phase. This phenomenon is sometimes referred to as the *high-β runaway*, but based on the findings of Ref. 1, *non-zonal transition* is considered to be a more suitable term.

It is to be stressed that technically, the NZT could occur without the decorrelation mechanism contributing to enhanced stochasticity—this could be the case if the even-parity component of $A_\parallel$ alone would be sufficiently strong to suppress the zonal flow. As will be discussed in the present paper, however, an NZT based solely on even-parity fluctuation suppression of zonal flows would effectively deplete the source of the even-parity $A_\parallel$, as the zonal flows moderate the corresponding energy transfer. Therefore, the system would return to the original state until the even-parity fluctuations have been replenished. Extreme heat flux levels are not expected to occur in this case.

In the following, a number of investigations performed in the context of the NZT are presented: After a few words on the gyrokinetic framework and the GENE code, which was used throughout this work, Sec. II provides details on the elaborate convergence studies conducted to ensure that the observed simulation features are not of an unphysical nature. Data from various codes are shown, demonstrating agreement regarding $\beta_{\mathrm{crit}}^{\mathrm{NZT}}$. A study of zonal flows follows in Sec. III, where flux-surface-breaking magnetic fluctuations are investigated in their impact on the zonal flow residual and geodesic acoustic modes (GAMs). This is done with

simplified models mimicking different degrees of realism of the fully turbulent scenario. Next, the field line integration routine used by the GENE DIAGNOSTICS TOOL is described and then applied to turbulence data in order to extract $\Delta r_{1/2}$. Before a summary of the findings of this paper, Sec. V follows which explores the nonlinear transfer of energy, with transfer occurring mainly from the unstable linear ITG mode to stable modes, catalyzed by the zonal flow—this property, however, is found to change as the NZT threshold is crossed. Two additional studies, related to secondary (zonal-flow-related) and tertiary instability growth, will be published separately—here, it suffices to say that the respective results are consistent with the interpretations provided below and in Ref. 1.

II. NUMERICAL FRAMEWORK AND CONVERGENCE

Gyrokinetic theory (see Ref. 5 and references therein) is well-established as an efficient and encompassing tool for the study of core microturbulence. The numerical implementation used here is the GENE code,[6,7] an extensively benchmarked (see, e.g., Refs. 8–11) Vlasov solver which, for the present investigations, was used in its radially local mode of operation. The set of physical parameters employed throughout most of this work is given in Ref. 12 and corresponds to the Cyclone Base Case (CBC).[13]

When focusing on new effects such as the NZT, ensuring numerical convergence is an essential task. As a baseline resolution, $(N_x, N_{ky}, N_z, N_{v\parallel}, N_\mu) = (192, 24, 24, 48, 8)$ was used which results in well-converged simulations (where convergence is measured in different transport channels, including the electron magnetic channel) for the parameters in Ref. 12. These resolutions correspond to the radial coordinate x, the binormal coordinate y, the coordinate z parallel to the background magnetic field, the parallel velocity $v_\parallel$, and the magnetic moment μ, respectively. For efficiency, some of the simulations in this work use a slightly reduced set of resolutions: $(128, 16, 16, 32, 8)$. These values yield qualitatively identical results with only very moderate quantitative differences, as corroborated by the fact that they mimic the resolutions used in Ref. 14, where simulation results for the same physical parameters are reported.

Just inside the NZT regime, i.e., at $\beta \gtrsim \beta_{\mathrm{crit}}^{\mathrm{NZT}} = 0.9\%$, numerical convergence was ensured thoroughly: all resolutions were doubled, quadrupled, or sometimes even increased six-fold, as were the box sizes $L_x, L_y, L_{v\parallel}$, and L_μ (at constant respective grid spacing), directly corresponding to the above coordinates—$L_z/(q_0 R_0)$ is always set to 2π. Here, q_0 is the safety factor and R_0 the major radius. The time step was reduced severely, and different (explicit) time stepping schemes were tested. A number of finite differencing schemes (including a conservative Arakawa scheme[15]) and numerical hyperdiffusion operators[16] were used, the latter in the parallel, parallel velocity, and radial direction, with the corresponding coefficients being varied over at least an order of magnitude. Additionally, simulations were performed both with and without parallel magnetic fluctuations $B_\parallel$ (in the following, $B_\parallel$ will be ignored). None of the above modifications resulted in the simulations saturating ad infinitum at regular heat fluxes or significantly affecting transient saturation transport levels or $\beta_{\mathrm{crit}}^{\mathrm{NZT}}$. It should be noted, however, that *under*-resolving the y direction only up to a maximum $k_y \sim 0.4$, i.e., with only half the minimum grid spacing, does indeed result in the transition shifting to higher β. This is readily explained by the fact that under-resolving y reduces the magnetic field stochasticity level B_x which is directly responsible for the threshold β value.

These findings are in line with those of other codes. Unfortunately, there exists little published material, as there has in the past been some uncertainty as to whether the NZT threshold may be a numerical artifact. In Ref. 17, a few cases are described. Reference 18 presents data from the gyrokinetic codes GYRO[19] and GKW[20] (the data of the former taken from Ref. 14), which is shown along with GENE curves in Fig. 1. The plotted data illustrates that the aforementioned codes agree well both regarding the saturated transport values at $\beta < \beta_{\mathrm{crit}}^{\mathrm{NZT}}$ and the NZT threshold β itself, further supporting the statement that the NZT is physical.

In the corresponding figure in Ref. 18, there are different GENE data points included in the high-β range which had been taken from Ref. 12. The authors of this latter publication had assumed at the time that the NZT is numerical in nature and had experimented with various initial conditions to avoid saturation transience—this was briefly commented on in Ref. 21 but warrants further explanation here. Initializing a simulation with $\beta > \beta_{\mathrm{crit}}^{\mathrm{NZT}}$ using the distribution function data from the nonlinear, saturated state at a β just below $\beta_{\mathrm{crit}}^{\mathrm{NZT}}$ results in saturation at the higher β for long phases, often many hundred time units R_0/c_s, with the ion sound speed c_s. The data shown in Ref. 12 illustrates that for these simulations, the electron magnetic heat flux—and thus the magnetic fluctuation level—is lower than one would expect when extrapolating from below $\beta_{\mathrm{crit}}^{\mathrm{NZT}}$. Therefore, it appears that the time scale for the turbulence to create stronger fluctuations and for those fluctuations to deplete the zonal flow

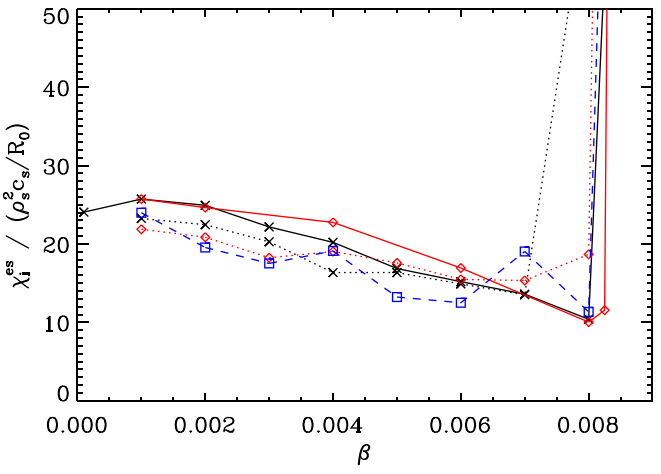

FIG. 1. Results from gyrokinetic codes GENE (black crosses), GYRO (red diamonds), and GKW (blue squares) for $\beta \leq \beta_{\mathrm{crit}}^{\mathrm{NZT}}$: plotted is the ion electrostatic heat diffusivity. The near-vertical lines at the threshold illustrate a transition to very large transport values; for all β scans shown, this occurs above $\beta = 0.8\%$ but below $\beta = 0.85\%$. Good quantitative agreement is found both for the pre-NZT transport and the NZT threshold. Dotted lines (GENE and GYRO) indicate sensitivity tests with slightly different numerical settings.

sufficiently to create an NZT can be relatively long. As a result, it is even possible to use standard initial conditions and perform simulations directly at even higher β, now very close to the kinetic ballooning mode (KBM) threshold $\beta_{\mathrm{crit}}^{\mathrm{KBM}}$ (where the KBM becomes linearly unstable), and obtain saturation for very long times—the linear ITG mode is sufficiently weak at these β values that the moment at which the NZT starts is shifted to much later times. This, in turn, demonstrates that there is indeed physical meaning to the transport values reported in Ref. 12, in particular close to the KBM threshold.

Supportive of these findings is the fact that for CBC parameters, the NZT is in some sense marginal. More specifically, there are two facets of these parameters to support that statement: First, $\beta_{\mathrm{crit}}^{\mathrm{NZT}} \approx 0.9\%$ is only a little smaller than $\beta_{\mathrm{crit}}^{\mathrm{KBM}} \approx 1.3\%$, meaning that for slightly lower background gradients, no transition is observed. Second, near the ballooning threshold, the (now subdominant) linear ITG mode is almost stabilized by finite β, and a trapped electron mode (TEM) is the dominant instability; consequently, the NZT time scale changes significantly.

Having demonstrated that the NZT is a very robust phenomenon with respect to numerical properties of the simulations, the focus is now shifted to physical aspects of ITG turbulence near the NZT threshold. First, the impact of magnetic fluctuations on zonal flows is studied.

III. ZONAL FLOWS AND MAGNETIC FLUCTUATIONS

In some brevity, Ref. 1 sketches an extension to the prevailing theory on zonal flow residuals,[22,23] where flux-surface-breaking radial magnetic fluctuations are causing a reduction of the amplitude of the residual. The full details of this new theory—along with a discussion of the underlying physics—will be presented in a separate paper, while here, additional details and background information with regard to the corresponding numerical setup are given. Note that the present work focuses only on the erosion of zonal flows whereas a study of the finite-β properties of their nonlinear drive has been relegated to a separate publication (Ref. 24)—it suffices to stress here that no impact of (moderately) changed zonal flow drive on the NZT is to be expected.

The analytical prediction for the behavior of the electrostatic potential Φ to which the numerical studies are compared reads

$$\Phi(t) \approx \Phi_{\mathrm{R}} - \mathcal{S}_{\alpha^2} t^2. \tag{1}$$

Here,

$$\mathcal{S}_{\alpha^2} = \frac{2\int \mathrm{d}^2 v_\perp F_0(v_\perp) \hat{S}_{\mathrm{e}}^{\Phi} \alpha^2}{(n_0 e/T_{\mathrm{i}0}) k_x^2 \rho_{\mathrm{s}}^2 \mathcal{R}}, \tag{2}$$

with

$$\Phi_{\mathrm{R}} = \frac{\Phi(t=0)}{1 + 1.6 q_0^2/\epsilon_{\mathrm{t}}^{1/2}} \equiv \frac{\Phi(t=0)}{\mathcal{R}} \tag{3}$$

and the electron source $\hat{S}_{\mathrm{e}}^{\Phi}$. Furthermore, $\alpha = A_\parallel k_x k_y v_{\mathrm{Th,e}}/B_0$, with the electron thermal velocity $v_{\mathrm{Th,e}}$. Additional definitions are as follows: e is the elementary charge, F_0 is the background Maxwellian, and B_0 the background magnetic field; T_{j0} denotes the background temperature of species j, and t is time; Lastly, ϵ_{t} denotes the inverse aspect ratio of the flux surface under investigation. For Eq. (1) to be valid, one requires $k_x^2 \rho_{\mathrm{s}}^2 \mathcal{R} \ll 1$ and $\alpha^2 t^2 \ll 1$.

A few comments are in order regarding how these findings apply to simulations. First, $\Phi_{\mathrm{R}} - \Phi(t) = \mathcal{S}_{\alpha^2} t^2 \propto \alpha^2 t^2$ in the limit of (moderately) short times. Second, the electron source $\hat{S}_{\mathrm{e}}^{\Phi}$ in Eq. (2) is directly related to the electron density at the (unmodified) residual which in turn is related to Φ_{R}. The $\alpha^2 t^2$ behavior of Eq. (1) agrees with the simulation results presented next. Third, using a constant-in-time $A_\parallel$ is necessary to avoid direct analytical treatment of nonlinear effects while constituting a significant simplification of the turbulent case.

It is straightforward to implement such a setup numerically, by replacing the self-consistent computation of $A_\parallel$ by some function of z and possibly t. Numerical studies of zonal flow decay and residuals typically have a single finite $|k_x|$, with only $k_y = 0$ (the zonal mode) being computed in a linear simulation. As the present objective is to analyze the impact of B_x fluctuations, nonlinear coupling to at least one finite-k_y mode is necessary. When $A_\parallel$ is kept fixed in time, the magnetic ($A_\parallel$) part of the nonlinearity reduces to a quasi-linear term, and only at large times t do self-consistent electrostatic coupling effects play a role—this temporal region is therefore excluded from all results shown here.

The way the initial condition for such runs is chosen can have a strong impact on how challenging the corresponding simulations are going to be numerically. Zonal flow studies of the type presented here are typically initializing a $(k_x, k_y) = (1, 0)$ mode in Φ which is constant in the parallel direction.[22,23] Here, $k = 1$ is meant to symbolize some finite value rather than specifically an inverse ion sound gyroradius. One thus obtains the full physics of the GAM damping, resulting in the usual residual Φ_{R} being eroded over time by the imposed B_x. As mentioned above, for B_x, a resonant, constant-in-time $A_\parallel$ is inserted at $(k_x, k_y) = (0, 1)$—and set to zero for any other (k_x, k_y)—which acts on the zonal flow through the Vlasov nonlinearity.

While this setup is very useful to demonstrate that both the GAM frequency and the GAM damping rate are unchanged by B_x (see Fig. 2), it is also clear from this plot that a quantitative analysis of the impact of B_x on the residual is made rather difficult by the presence of the GAMs, even ignoring the stringent resolution requirements in velocity space stemming from the need to resolve these modes (for the curves in this plot, $N_{v\parallel} = 128$ and $N_\mu = 32$ were used, along with $N_z = 24$; doubling these values changes neither the GAM frequency, the GAM damping, nor the zonal flow damping with B_x). In the figure, larger B_x are shown to have a stronger reducing effect on the residual. Two different approaches are detailed below, both of which allow for a more precise analysis of this property.

First, one may start a simulation with $A_\parallel = 0$, which will eventually yield the unmodified, constant-in-time Φ_{R}; by applying a moderate collision frequency ν_{c} and/or

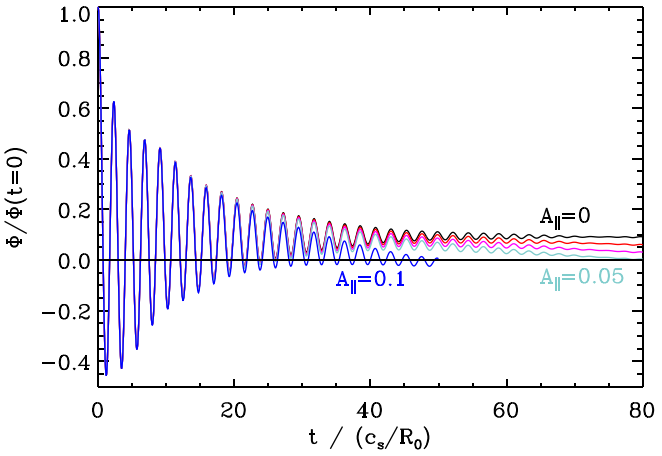

FIG. 2. GAM oscillations and zonal flow damping for various, increasing values of the resonant, artificially imposed $A_\parallel$. Shown is the electrostatic potential as a function of time, normalized (separately for each curve) to its value at $t = 0$. Stronger magnetic fluctuations result in faster decay of the residual, with the linear dependence predicted by Eq. (1) visible in the simulation data. For $A_\parallel = 0$, the usual residual Φ_R is retained.

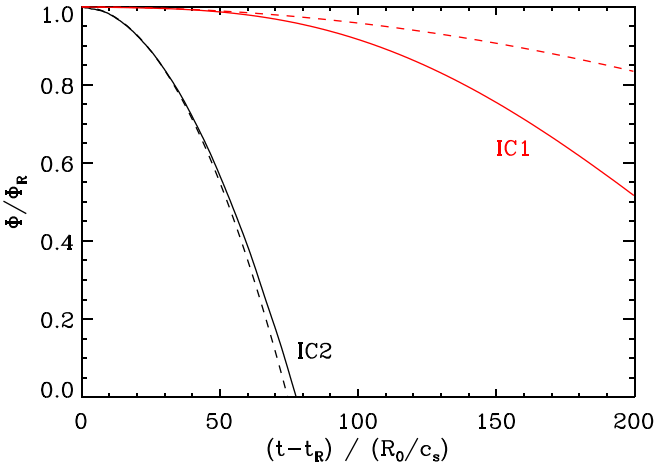

FIG. 4. Decay of the zonal flow residual due to resonant magnetic fluctuations, for two different initial conditions labeled IC1 (red) and IC2 (black). Here, the initial oscillatory phases were computed without B_x, and moderate collisionality and/or $v_\parallel$ hyperdiffusion were used during $t < t_R$ to reduce the velocity space fine structure more quickly. A quadratic fit (dashed curves) was obtained for IC2 which also applies to IC1 when rescaled appropriately. Both curves start to deviate from the quadratic fit curves near $t - t_R \approx 70R_0/c_s$.

hyperdiffusion D_v in $v_\parallel$ (but no D_z),[16] the fine structure in the ion velocity space (see Fig. 3) introduced by the GAMs can be smoothed out more quickly, while introducing only a slow, linear-in-time decay of the residual. At a time when the GAM oscillations have disappeared but Φ_R is still reasonably conserved, ν_c and D_v are reduced to zero; subsequently, B_x is switched on at some finite value. Now, the magnetic-fluctuation-induced effect on the residual can be seen much more clearly, see the red curve labeled IC1 in Fig. 4: the quadratic dependence on t as predicted by Eq. (1) for moderate times t is recovered.

However, this approach does not alleviate the constraining nature of the resolution requirements; and remnants of velocity space fine structure can make it difficult to obtain smooth curves such as the one labeled IC1 in Fig. 4. Therefore, a different setup—corresponding to the label IC2 in the same figure—is described which allows for much more efficient studies of parameter dependencies and of the properties and convergence of the B_x effect. Moreover, with IC2, clear results without remnant features from polluting effects such as the GAMs or collisions/hyperdiffusion can be obtained.

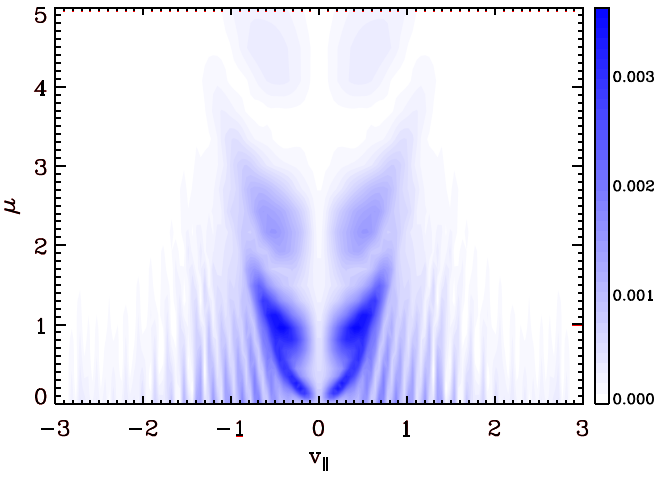

FIG. 3. Ion distribution function $|f|$ in velocity space (not the entire μ domain is shown here), at the outboard midplane. The fine structure dominating the plot is a result of the GAM oscillations (see also Ref. 25), and the need to resolve it can make simulations rather expensive. This snapshot was taken from the simulation labeled $A_\parallel = 0$ in Fig. 2 at $t = 37.4R_0/c_s$; for the curve with the smallest finite $A_\parallel$, the plot for $|f|$ is visually indistinguishable from the one shown here.

While for zonal flow studies with adiabatic electrons, there is no difference between initializing the $(k_x, k_y) = (1, 0)$ mode in n_i or in Φ, this is no longer the case for kinetic electrons. Initializing n identically for both ions and electrons (IC2), rather than the electrostatic potential (IC1), now results in $\Phi(t)$ oscillating in a GAM-like manner and then approaching a residual which is no longer described well by the theoretical prediction for $\Phi_R/\Phi(t = 0)$. In particular, the residual now lies above $\Phi(t = 0)$ rather than significantly below it for CBC parameters—hereafter, Φ_R in the context of IC2 is meant to refer to the actual residual in this case rather than the theoretical prediction in Eq. (3). Moreover, while the electrons in IC2 have a very similar distribution compared with the post-GAM residual state of IC1 for large times t, the ions are at that point close to Maxwellian (see Fig. 5).

The new setup IC2 results in the simulations becoming significantly less expensive in terms of computation time, as the GAM physics no longer require to be resolved. This approach, however, is only useful if one is interested purely in the dynamics of the system once the residual state is reached (and the original state at $t = 0$ is no longer relevant), as is the case in the present work. Note that since the previously described analytical theory relies on electron motion for the quadratic reduction of $\Phi(t)$, the differences in the ion distributions are expected not to matter, at least for moderate times t.

The strategy employed here is to use the second initial condition IC2 and do spot checks to ensure that the results in the phase where B_x is active—for $t \geq t_R$—are equivalent to

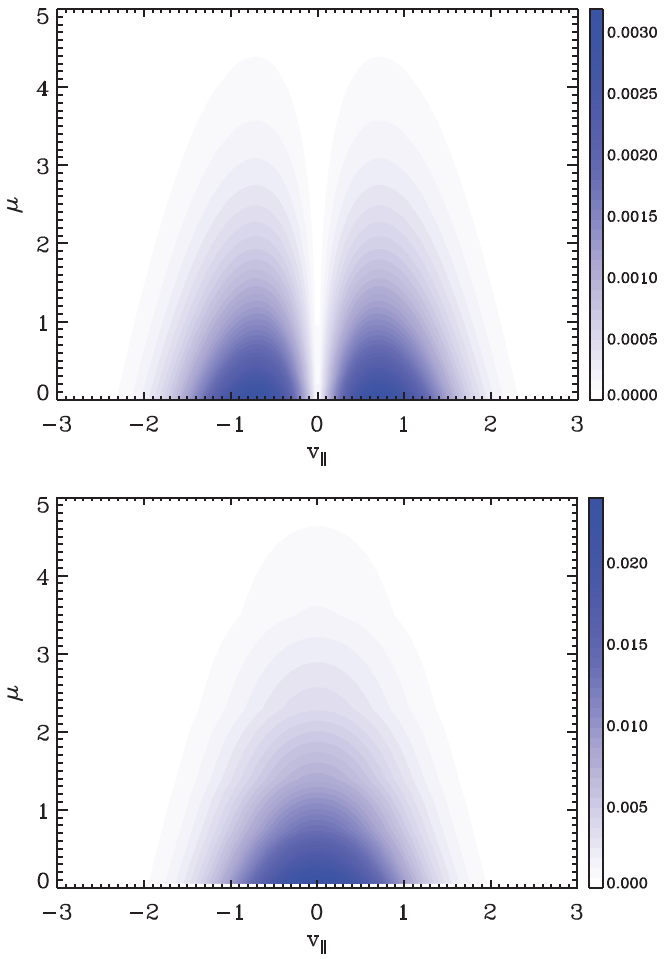

FIG. 5. Ion distribution function $|f|$ in velocity space for the standard initial condition IC1 (top) and the alternate version IC2 (bottom) designed to obtain cleaner results with less computational effort. Both plots represent snapshots after the respective oscillating phase has died down, at the moment when B_x is turned on. The difference does not influence zonal flow decay due to B_x; however, the specific shape of the ion distribution does not enter into the analytical calculation. The corresponding electron distributions are almost identical qualitatively for both initial conditions.

those obtained through the first initial condition. Fig. 4 illustrates that the results do indeed agree very well when taking into account the different electron source. Similarly to the zero-crossing time $t_{\Phi=0}$ (Ref. 1) as a measure for the impact of B_x, one may define a factor η, with $\Phi(t-t_\mathrm{R})/\Phi_\mathrm{R} = 1-\eta(t-t_\mathrm{R})^2$. This corresponds to the form in Eq. (1), with one important difference: the quadratic decay in Eq. (1) is proportional to $\hat{S}_\mathrm{e}^\Phi \sim n_\mathrm{e}(t=0) \sim n_\mathrm{e}(t=t_\mathrm{R})$, where here it scales like $\Phi(t=0) \propto \Phi_\mathrm{R}$. As both initial conditions use different ratios of the electron density n_e to Φ, this ratio must be taken into account when comparing results from IC1 and IC2. In Fig. 4, the same parameters (including B_x) were used for both curves, but they differ by a factor

$$\mathcal{F}_n^\Phi = \left[\frac{\Phi_\mathrm{IC1}/n_\mathrm{e,IC1}}{\Phi_\mathrm{IC2}/n_\mathrm{e,IC2}}\right]_{t=t_\mathrm{R}}. \tag{4}$$

To obtain the dashed fit curves in Fig. 4, the curve for IC2 was fitted with an inverse parabola, and the corresponding η_IC2 was then multiplied by $\mathcal{F}_n^\Phi = 43.4$ to obtain η_IC1. The latter, for moderately short times t, can be seen to constitute a reasonably good fit (for moderately short times $t - t_\mathrm{R} \lesssim 70$) to the data resulting from fully resolving the GAM phase.

Parameter scans based on IC2 reveal, in addition to the aforementioned properties, that the corresponding simulations are well-converged in all numerical parameters (with respect to $t_{\Phi=0}$ and thus η) at resolutions of $(N_{v\parallel}, N_\mu) = (48, 8)$ and that the exact shape of $A_\parallel$ along the z coordinate is irrelevant: only its average $\langle A_\parallel \rangle_z$ influences $t_{\Phi=0}$. Furthermore, imposing B_y rather than B_x causes the decay to vanish altogether while introducing complex fluctuating behavior of $\Phi(t)$ without changing the statistical average in time. All of these findings are in accordance with the theory and its physical interpretation.

Reference 1 reports the damping strength due to B_x by giving the parameter dependencies of the zero crossing of the potential, yielding $t_{\Phi=0} \propto q_0 \epsilon_\mathrm{t}^{-1/6} k_x^0 B_x$. The crucial dependencies for k_x and B_x (the same holds for q_0) can be recovered from Eq. (1) by setting $\Phi(t) = 0$. For the inverse aspect ratio, the theory prediction is $\epsilon_\mathrm{t}^{-1/4}$ it is possible to recover this value in more careful analyses of numerical studies, as will be demonstrated in the aforementioned separate paper.

Quantitative comparisons between the analytical approach and the simulations (for sufficiently short times) yield agreement to within about 15%. Improving this number would likely require a more involved treatment, making the analytical calculations much more difficult or even impossible. The behavior of the damping with respect to the important parameters B_x, q_0, and $T_\mathrm{i}/T_\mathrm{e}$ is reproduced accurately, however. More details will be given in the aforementioned separate paper.

The significant disparity of magnitude between Φ_IC1 and $n_\mathrm{e,IC1}$ is responsible for the large value of $\mathcal{F}_n^\Phi = 43.4$. Therefore, the following quantitative application to realistic cases of turbulence will be based on IC2. Since the claims made in this work regarding the NZT rely on zonal flow decay to occur on time scales comparable with or faster than other relevant time scales in the system, it is instructive to compare $t_{\Phi=0}$ with the spatially averaged turbulent correlation time t_corr which is defined as the time at which the autocorrelation function of the electrostatic potential

$$C_\Phi(t) = \frac{\sum_{t'} \langle \Phi(t')\Phi(t'+t)\rangle_{x,y,z}}{\sum_{t'} \langle \Phi(t')^2\rangle_{x,y,z}} \tag{5}$$

has decayed to $\mathrm{e}^{-1} = 0.368$. To this end, measurements are taken at $\beta = 0.7\%$ (covering the entire quasi-stationary state). One obtains $t_\mathrm{corr} = 5.9 c_\mathrm{s}/R_0$ and a resonant $B_x = 0.026$, mainly stemming from the low-k_y region. To estimate $t_{\Phi=0}$, one can directly compare with the (appropriately scaled) data in Ref. 1, thus arriving at $t_{\Phi=0} = 3.2 c_\mathrm{s}/R_0$—indeed a value relatively close to but smaller than t_corr. Therefore, at this point just below $\beta_\mathrm{crit}^\mathrm{NZT}$, the resonant components of B_x already play some role in the dynamics of the zonal flows—not surprisingly, as the shearing rate is already subjected to major modifications at that β.[12] It is intuitive that with the sudden addition of another very stochastic B_x component, the turbulent system will react rather strongly.

While the use of a time-independent B_x allows for comparisons with the analytical approach as well as convenient isolation of the underlying physical effect, it is possible to choose a slightly more realistic setup: The standard Rosenbluth-Hinton scenario relies on a dynamics focused solely on the $k_y = 0$ mode and is thus unable to create any appreciable B_x self-consistently. To mock up a nonlinear coupling between B_x and the distribution function, the magnetic fluctuations are scaled with the magnitude of Φ, as illustrated in Fig. 6, which shows simulations based on IC2. The response of the zonal flow is to decay quasi-exponentially, with the t^2 dependence preserved for short times, the decay occurring on a similar time scale as in the case with constant-in-time B_x.

The attention of the reader is now turned to magnetic field lines and how their decorrelation can provide amplified flux-surface-breaking magnetic fluctuations whose impact on zonal flows has been studied in this section.

IV. MAGNETIC FIELD LINE INTEGRATION

A. Numerical details

As part of the GENE DIAGNOSTICS TOOL,[26] a routine is available to integrate field lines from the $A_\parallel$ grid data and produce either Poincaré plots or calculate magnetic diffusivities. Its functionality and algorithmic properties are described below.

First, the initial positions of the field lines to be traced are fixed; unless specified otherwise, the rectangular seed position grid is centered in both the x and y direction about the middle of the box, where the box ranges from $-L_x/2$ to $L_x/2$ and from $-L_y/2$ to $L_y/2$, with the number of seed lines in x and y being free parameters. Note that lines with the same x but different y lie on the same (unperturbed) flux surface. For most studies of turbulent field line behavior and throughout this work, lines are all seeded equidistantly along the line of $y = 0$.

Next, the (Fourier space) input data for $A_\parallel$ is extended in the parallel direction, using the parallel boundary condition

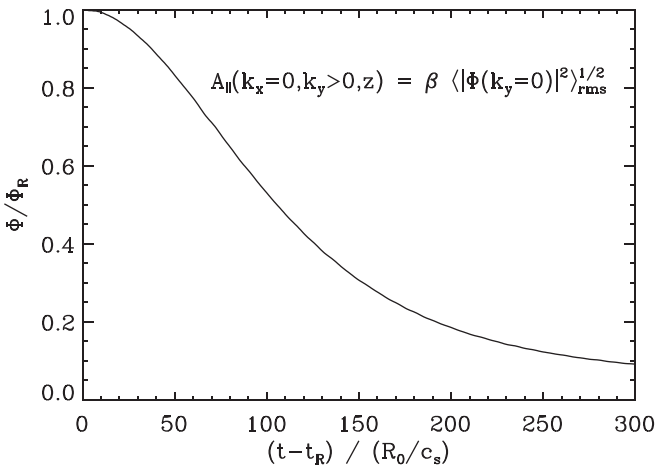

FIG. 6. Zonal flow decay for magnetic fluctuations scaled with the magnitude of Φ as prescribed in the figure. In the parallel direction, $A_\parallel$ is set to be constant, as only the constant component will contribute to the erosion of the zonal flow. This simulation uses IC2 and the same parameters as in Fig. 4.

$$A_\parallel(i,j,+\pi) = (-1)^{j\mathcal{N}} A_\parallel(i + j\mathcal{N}, j, -\pi), \tag{6}$$

where i and j are the mode numbers corresponding to k_x and k_y, respectively, and $\mathcal{N} = 2\pi\hat{s}L_x/L_y$. Additionally, the magnetic potential is normalized to $B_0(z)$, which, in $\hat{s}$-α geometry,[27] reads $B_0(z) = 1/(1 + \epsilon_t \cos z)$. The resulting data is then interpolated linearly along the parallel coordinate, typically to at least 128 grid points. Note that this interpolation is performed with the $A_\parallel$ data still in Fourier space in x and y, which numerically preserves $\nabla \cdot \mathbf{B} = 0$. Next, k_x and k_y are multiplied onto $A_\parallel$ to arrive at B_y and B_x, respectively. With the magnetic fields thus interpolated parallelly, Fourier transforms are applied to the perpendicular directions, and—if necessary—Fourier interpolation is used to increase the perpendicular real space resolutions.

The next step comprises the actual integration: starting at the inboard (i.e., at parallel position $z = -\pi$), all lines are advanced in steps of Δz, and after every completed poloidal turn, the positions are recorded, as are any applications of the (periodic) radial boundary condition to allow for the correct evaluation of the diffusivity. All steps follow this scheme: The local B_x and B_y are evaluated at the field line position through linear two-dimensional interpolation between perpendicular grid cells, where they specify the displacement of the field line per Δz according to

$$(x,y)[z + \Delta z] = (x,y)[z] + \frac{2\pi q_0 R_0 B_{(x,y)}}{N_z B_0}. \tag{7}$$

Rather than simply taking this to be the next parallel position, only half a parallel step is taken, and the values for $B_{(x,y)}$ obtained at the half-way position are used to advance the field lines from z to $z + \Delta z$. This predictor-corrector method is employed to reduce errors due to field line curvature. Whenever a field line arrives at a simulation domain boundary, it is mapped back into the local flux tube. This scheme is fairly efficient, and $\mathcal{O}(100)$ field lines can be traced at typical resolutions for 100 poloidal turns per second.

The Poincaré data can be visualized by drawing a single point per recorded position at the outboard midplane ($z = 0$), where the points are colored by seed position. As a result, flux surface intactness may be measured by a separation of colors, whereas thoroughly mixed colors indicate efficient flux surface destruction (see Fig. 7 for an example similar to results presented in Ref. 28). Alternatively, Poincaré histograms may be plotted, counting the number of field lines per x-y bin, which can offer clearer pictures for large numbers of lines and/or poloidal turns.

To provide a quantitative measure of the field line behavior, a diffusivity may be computed as follows. The radial displacement of line l after one poloidal turn p is $\Delta r(l,p) = r(l,p) - r(l,0)$, leading to a definition very similar to the one in Ref. 4 of the field line diffusivity

$$D_{\mathrm{fl}}(l,p) = \frac{\Delta r(l,p)^2}{2\pi q_0 R_0 (p+1)}, \tag{8}$$

where l covers only distinct radial seed positions. In other words, if multiple lines are seeded in y per x position, their

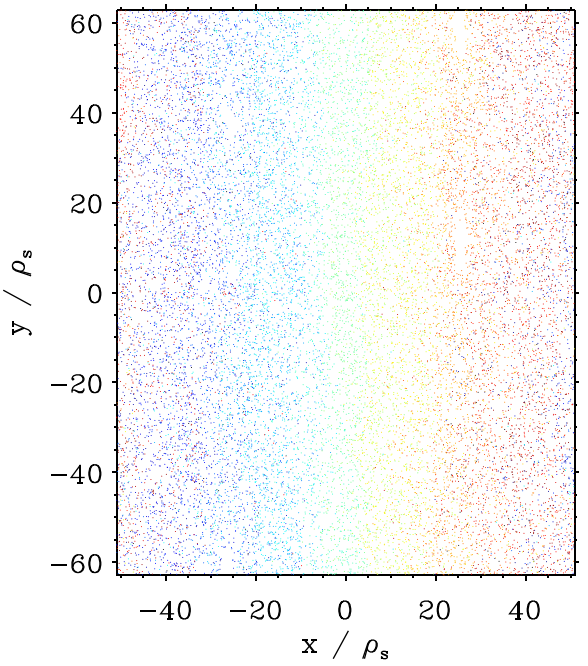

FIG. 7. Poincaré section (inboard midplane) for the same simulation data as in Fig. 9 at $t = 328.8$. Different colors correspond to different seed positions of the field lines (all seeded at $y = 0$), out of a total of 200 lines traced for 100 poloidal turns. The mixing of colors indicates a strongly stochastic field.

radial displacement is averaged over before computing $D_{\mathrm{fl}}(l,p)$. One can now plot both $D_{\mathrm{fl}}(p)$ for a single l or averaged over all lines, as illustrated in Fig. 8. This quantity typically converges after a few ten poloidal turns and shows little variation after that point, provided a statistically sufficient number of seed lines in x was used.

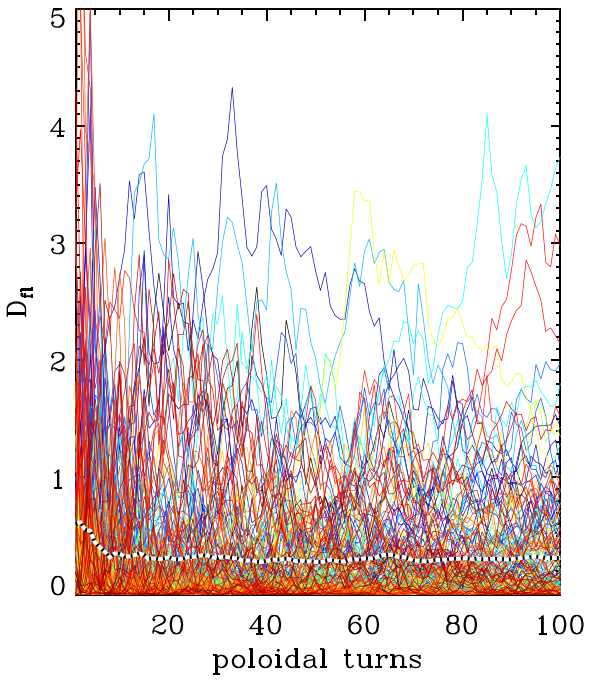

FIG. 8. Field line diffusivity as a function of the poloidal turn number; different colors correspond to different field lines. The black-and-white dotted line marks the average over field lines: after an initial phase where lines move ballistically, the stochastic (diffusive) regime is reached, and D_{fl} saturates. See the caption of Fig. 7 for more details.

While the entire above formalism is applied to the $A_{\parallel}$ data for a single time step of the simulation, it is now easily extended in order to provide temporal statistics, yielding a time-averaged value $D_{\mathrm{fl,avg}}$.

Results from this routine have been published in Refs. 3 and 29–32, in addition to Ref. 1. The latter required a small modification, namely, stopping the integration at the outboard midplane, i.e., after half the z points had been integrated over, and storing the radial position at that point to compute $\Delta r_{1/2}$.

B. Application to field line decorrelation and the NZT

Using the field line diagnostic on turbulence data to determine $\Delta r_{1/2}$ in the context of field line decorrelation leaves one question to be addressed: Which is the critical field line to decorrelate? While the correlation length λ_{Bxx}, taken at the outboard midplane, is well-defined, the most-displaced field line will decorrelate much more easily than the least-displaced one (which, in fact, is unlikely ever to decorrelate). As the aim here is to identify the critical β where odd-parity B_x first becomes flux-surface breaking, the first field line to decorrelate is of essential interest. It is therefore important to show that $\Delta r_{1/2}$ for this field line is statistically well-defined.

Possible definitions for $\Delta r_{1/2}$ for ensembles of field lines include: the displacement of the most-displaced field line, that which is exceeded by exactly 10% of all field lines, and that which is exceeded by a fraction of $\mathrm{e}^{-1} \approx 0.37$ of the entirety of lines. Fig. 9 shows results based on these three definitions as functions of time for a β value of 0.7%, in addition to the average displacement. Clearly, all four are in a quasi-stationary equilibrium, and the ratio of the $\Delta r_{1/2}$ for any two quantities can be expressed by a constant-in-time factor at all times. It is thus demonstrated that the most-displaced field line can indeed be employed for comparison with λ_{Bxx} without causing concern regarding random fluctuations of a single traced line. Note that to ensure that this field line is

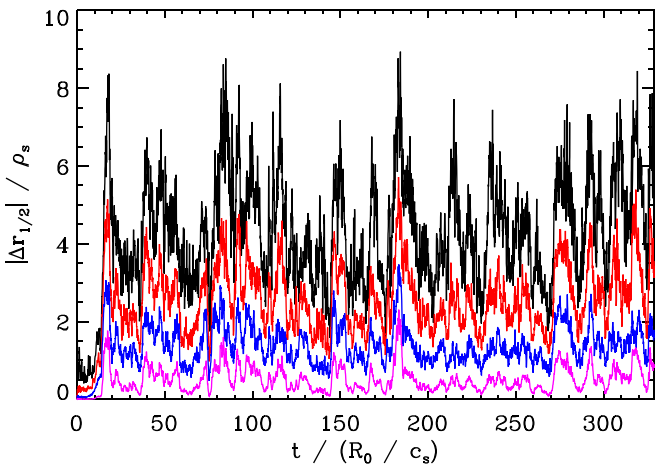

FIG. 9. Radial displacement $\Delta r_{1/2}$ of field lines as a function of time, at the outboard midplane for CBC parameters at $\beta = 0.7\%$. From top to bottom, the curves correspond to the displacement exceeded by the most-displaced field line (black), the 10% most-displaced field lines (red), the e-fold fraction (blue), and the average displacement of all lines (pink). For these curves, 1000 lines were traced.

indeed the most-displaced line in the system, the total number of lines needs to lie well above N_x for a given (numerically converged) simulation.

Fig. 10 shows $\Delta r_{1/2}$ as a function of β. As λ_{Bxx} typically does not vary too drastically with β, and as $\Delta r_{1/2} \propto \beta$, one should always be able to find an intersection of these two curves, at which point in most cases an NZT should occur. However, the β value at which the curves intersect may lie above the KBM threshold, making the NZT threshold unobservable in both simulations and experimental studies for these cases.

It may be possible to derive a model which estimates $\Delta r_{1/2} \sim B_x$ from a quasilinear description of the heat diffusivity via the relation described in Ref. 33 and then compare that value to an estimate of the radial correlation length of B_x. This, however, would exceed the scope of the present work.

While Fig. 10 provides a convincing argument for the NZT mechanism for CBC parameters, it is important to verify whether the same holds when looking at different parameter regimes. An NZT also occurs for GA-standard case[34] parameters—see Refs. 17 and 24 for more details. In Fig. 11 (upper plot), the results of an analysis akin to that of Fig. 10 (and using the same definition for $\Delta r_{1/2}$) are shown: again, the intersection of the radial half-turn displacement with the correlation length coincides very well with $\beta_{\text{crit}}^{\text{NZT}} = 0.3\% < \beta_{\text{crit}}^{\text{KBM}} \approx 0.7\%$. Another case, this time based on density-gradient-driven TEM turbulence where zonal flows play an important role in regulating the transport levels (see Ref. 21) is shown in Fig. 11 (lower plot). Here, the KBM limit lies at $\beta_{\text{crit}}^{\text{KBM}} = 2.0\%$, and nonlinear simulations show no unexpected behavior between $\beta = 0\%$ and this threshold. In the figure, the intersection of the curves lies well above $\beta_{\text{crit}}^{\text{KBM}}$, consistent with the statement that no NZT occurs. Two points need to be noted, however. First, upon reaching the KBM regime, both half-turn displacement and correlation length can change although the former does not exceed the latter for stably saturated KBM simulations (not shown in the figure). Second, this second parameter case involves

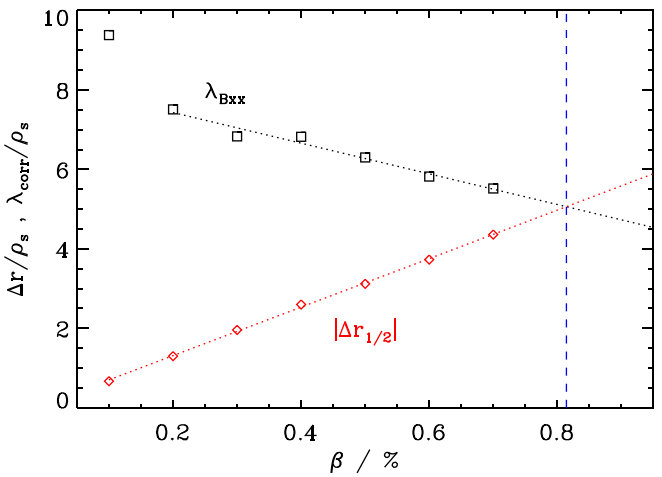

FIG. 10. Half-turn field line displacement $\Delta r_{1/2}$ (black squares; based on the definition involving the most-displaced field line) and radial correlation length λ_{Bxx} (red diamonds) as functions of β. The corresponding fit lines intersect at $\beta_{\text{crit}}^{\text{NZT}}$.

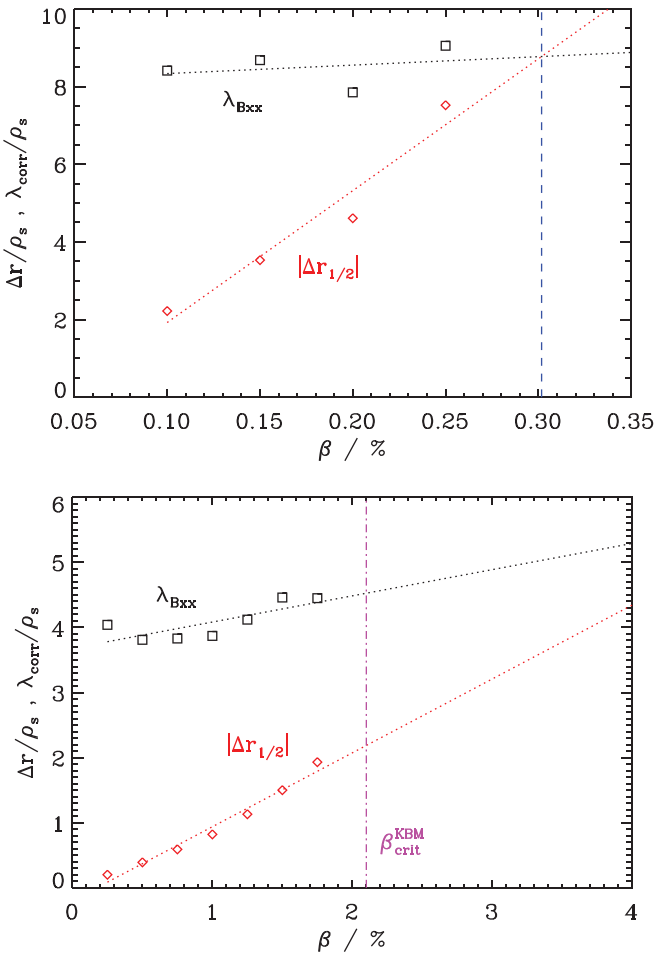

FIG. 11. Field line half-turn displacement and radial correlation length of B_x (same nomenclature as in Fig. 10) for GA-standard (upper plot) and TEM case parameters (lower plot). In the first case, the intersection occurs at the NZT threshold (blue dashed line) as expected, whereas in the second it has moved well beyond the KBM threshold (purple dash-dotted line), and no NZT is detected. Both plots use the same definition for $\Delta r_{1/2}$ as in Fig. 10.

TEM turbulence, so instead of a transition to extreme heat flux levels, an NZT would manifest itself merely via strongly reduced zonal flow activity and suddenly but not excessively increased transport—neither of these properties is found in the simulations.

Based on these findings, one can state that both the GA-standard and the TEM case are consistent with the proposed mechanisms of the NZT as well as with the quantitative definition of $\Delta r_{1/2}$ based on the most-displaced field line.

Field line decorrelation can be employed to understand certain other properties of the NZT, as shall be demonstrated in Sec. IV C.

C. Subdominant microtearing (SMT)-aided decorrelation

SMT excitation,[3] which appears to be ubiquitous in ITG turbulence, is responsible for the creation of resonant magnetic perturbations. These linearly stable modes receive energy from the linear ITG mode through three-wave interaction with the zonal flow. The distinguishing feature of SMT modes is that they produce even-parity $A_\parallel$ fluctuations, making them responsible for electron magnetic flutter

transport. One question arising in the context of the NZT is whether a transition can still occur if the SMT effect is suppressed.

As $\Delta r_{1/2}$ is determined by both even- and odd-parity contributions to B_x, and as removing SMT modes from the system will effectively eliminate any even-parity B_x, this procedure automatically reduces $\Delta r_{1/2}$, an effect visible in Fig. 12. Consequently, the intersection of $|\Delta r_{1/2}|$ and λ_{Bxx} (see Fig. 10) will be shifted to higher β, possibly even past $\beta_{\mathrm{crit}}^{\mathrm{KBM}}$. Therefore, it is appropriate to refer the process of lowering $\beta_{\mathrm{crit}}^{\mathrm{NZT}}$ through SMT activity as *SMT catalyzation*.

A comment is in order on the parity filtering applied to the data on which Fig. 12 is based: The unmodified simulation is used, and its $A_\parallel$ data is filtered in post-processing. While filtering of a linear mode centered on $k_x = 0$ is straightforward to implement via $A_\parallel(k_x, z) \to (A_\parallel(k_x, z) - A_\parallel(-k_x, -z))/2$, the nonlinear box poses a problem. One can either filter only the k_x modes connected with $k_x = 0$ through Eq. (6), filter for every k_x separately, or apply it to groups of connected k_x with many symmetry points occurring at off-center k_x (in cases where a given k_x is not connected to $k_x = 0$). Fig. 12 demonstrates for the first (red crosses) and second (blue squares) option that the outcome in terms of $\Delta r_{1/2}$ can be drastically different: the first results in only a very small reduction of the displacement, while the second causes it to drop to about 2/3 of the original value.

The problem of finding an appropriate filter choice is even more consequential when filtering the potential at runtime during a simulation: here, both the linear and nonlinear dynamics of the turbulence can be affected severely. Various attempts have yielded some small insights but no conclusive overall picture to aid in the understanding of the NZT; therefore, no results are reported in this publication.

Along the above lines, it may be speculated that applying external magnetic perturbations to the plasma will influence the NZT threshold, as well. Unless they change the linear mode behavior (e.g., through ITG suppression), and presuming they do not cancel the SMT-induced resonant B_x, they can be expected to contribute to the picture by enhancing $\Delta r_{1/2}$ and thus lowering $\beta_{\mathrm{crit}}^{\mathrm{NZT}}$.

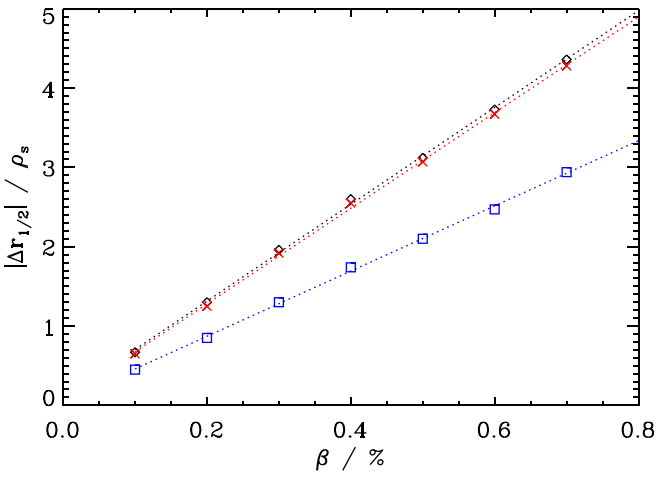

FIG. 12. Half-turn field line displacements $\Delta r_{1/2}$ of the most-displaced lines as functions of β for the unmodified simulation data (black diamonds); with even-parity $A_\parallel$ filtered out for $k_x = 0$ and connected k_x (red crosses); and with even-parity $A_\parallel$ filtered out for all k_x (blue squares). The reduction (but not elimination) of the displacement in the two latter cases (especially the last one) supports the concept of SMT catalyzation (see the text).

The near-marginal NZT cases in Refs. 12 and 21 also highlight another interesting property: It is possible to create scenarios where an NZT occurs at some value of β, but then disappears again due to lack of linear ITG drive when increasing β, before the ballooning threshold is reached. The reason lies in the fact that the NZT requires a linear mode that needs zonal flows to saturate. If, however, finite-β effects stabilize an ITG mode linearly at $\beta_{\mathrm{stable}}^{\mathrm{ITG}}$, and assuming one has $\beta_{\mathrm{crit}}^{\mathrm{NZT}} < \beta_{\mathrm{stable}}^{\mathrm{ITG}} < \beta_{\mathrm{crit}}^{\mathrm{KBM}}$, then an island of stability is created where there is either virtually no turbulent transport or possibly a different dominant instability (such as TEM) observed nonlinearly.

Next, a closer look is taken at the energetics near the NZT threshold.

V. NONLINEAR ENERGY TRANSFER

The modified zonal flow dynamics can be elucidated and quantified by examining nonlinear energy transfer functions[35,36] for β below and above the NZT threshold. To this end, the free energy is defined as[37–39]

$$E_{\mathbf{k}} = \sum_j \int \mathrm{d}z \mathrm{d}v_\parallel \mathrm{d}\mu \, \frac{T_{j0}}{F_{j0}} \left(g_{j\mathbf{k}} + q_j \frac{F_{j0}}{T_{j0}} \chi_{j\mathbf{k}} \right)^* g_{j\mathbf{k}}, \tag{9}$$

where j denotes the particle species, q_j is particle charge, F_{j0} is the background Maxwellian distribution, $\chi_j = \bar{\Phi}_j + v_{\mathrm{Th},j} v_\parallel \bar{A}_{\parallel j}$ is the generalized potential, with the overbar denoting a gyroaverage and $v_{\mathrm{Th},j}$ being the particle thermal velocity. Note that the above definition can be rewritten to give the following expression:

$$E_{\mathbf{k}} = \sum_j \pi B_0 n_{j0} T_{j0} \int \mathrm{d}z \left(\int \mathrm{d}v_\parallel \mathrm{d}\mu \, \frac{|f_{j\mathbf{k}}|^2}{2F_{j0}} + \frac{\lambda_{\mathrm{D}}^2 k_\perp^2}{2} |\phi_{\mathbf{k}}|^2 + \sum_j \frac{n_{j0} q_j^2}{2T_{j0}} [1 - \Gamma_0(b_j)] |\phi_{\mathbf{k}}|^2 + \frac{k_\perp^2}{\beta} |A_{\parallel \mathbf{k}}^2|^2 \right), \tag{10}$$

where λ_{D} is the Debye length and $\Gamma_0(b_j)$ relates to the modified Bessel function $I_0(b_j)$ of argument $b_j \sim k_\perp^2$ (see, e.g., Ref. 16).

The nonlinear contribution to the evolution of the free energy at wavenumber k is defined by the sum over $\mathbf{k}'$ of the nonlinear transfer function

$$\mathcal{N}_{\mathbf{k},\mathbf{k}'} = \sum_j \int \mathrm{d}z \mathrm{d}v_\parallel \mathrm{d}\mu (k_x' k_y - k_x k_y') \times \left(q_j \chi_{j\mathbf{k}}^* \chi_{j\mathbf{k}'} g_{j\mathbf{k}-\mathbf{k}'} - q_j \chi_{j\mathbf{k}}^* \chi_{j\mathbf{k}-\mathbf{k}'} g_{j\mathbf{k}'} - \frac{T_{j0}}{F_{j0}} g_{j\mathbf{k}}^* \chi_{j\mathbf{k}-\mathbf{k}'} g_{j\mathbf{k}'} + \frac{T_{j0}}{F_{j0}} g_{j\mathbf{k}}^* \chi_{j\mathbf{k}'} g_{j\mathbf{k}-\mathbf{k}'} \right). \tag{11}$$

Here, the modified distribution function of species j at wavenumber $\mathbf{k}$ is denoted by $g_{j\mathbf{k}'}$ (see, e.g., Ref. 16). Of particular interest here is the nonlinear transfer function at $k_y' = k_y$ and

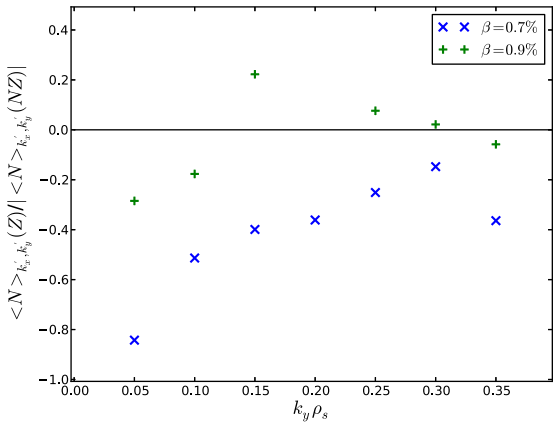

FIG. 13. Free energy transfer due to zonal flow coupling $\sum_{kx'} \mathcal{N}_{(kx,ky),(kx',ky'=ky,0)}$ (normalized to the total non-zonal energy transfer) for $\beta < \beta_{\text{crit}}^{\text{NZT}}$ (blue crosses) and $\beta > \beta_{\text{crit}}^{\text{NZT}}$ during the runaway phase (green pluses). The negative values for the former case indicate energy transfer via the zonal flows to higher k_x, consistent with the zonal flow shearing paradigm. In the latter case, the zonal coupling is much weaker or even positive, illustrating that the zonal flow dynamics are fundamentally altered and now contribute to the growth at some k_y.

$k_y' = 0$ since these combinations represent three-wave coupling with zonal flows. The standard zonal flow paradigm[40] describes the effect of zonal flows as a shearing mechanism that decreases the radial correlation length of turbulent eddies. In a nonlinear transfer function, the analogous effect is manifest as energy transfer from a given $\mathbf{k}$ to a $\mathbf{k}'$ with larger radial wavenumber and the same binormal wavenumber: $(k_x' > k_x, k_y' = k_y)$.[35,36] Therefore, $\mathcal{N}_{\mathbf{k},\mathbf{k}'}$ is examined for a series of wavenumbers at both $\beta = 0.7\%$ (below the NZT threshold) and $\beta = 0.9\%$ (above the threshold and during the runaway phase). The usual zonal flow shearing effect is clearly identified in the turbulence in the former case, whereas in the latter, the relative zonal flow coupling is much weaker and actually constitutes a net energy *source* for some wavenumbers. This is shown in Fig. 13, where the zonal flow component $\sum_{kx'} \mathcal{N}_{(kx,ky),(kx',ky'=ky,0)}$ of a series ($k_x = 0$ and $k_y = [0.05 - 0.35]$) of nonlinear transfer functions is plotted for the cases above and below $\beta_{\text{crit}}^{\text{NZT}}$. In the figure, the nonlinear transfer functions are normalized to the total non-zonal energy transfer in order to indicate the relative importance of the zonal-flow-related transfer. As described above, for $\beta = 0.7\%$, the values are negative, indicating that zonal flows are facilitating energy transfer to smaller radial scales. For the case with $\beta = 0.9\%$, at low k_y the values are still negative but are relatively much weaker. Then the zonal coupling reverses sign, indicating that during the NZT, the zonal flows reverse their role and contribute to the growth after the transient saturation phase.

VI. SUMMARY

A number of studies has been presented in this work, all of which aim to corroborate the picture of the NZT described in Sec. I and in Ref. 1. To this end, extensive numerical convergence checks and tests with different numerical schemes had been performed, where the NZT threshold was shown to be a numerically very stable phenomenon, underscoring its physical nature.

NZT physics were then investigated thoroughly. An analytical theory—adding radial magnetic perturbations to the standard approach for zonal flow studies[22,23] was successfully tested by means of simulations, demonstrating that a flux-surface-breaking B_x is able to destroy zonal flows through a decay process quadratic in time when B_x is held fixed. The influence of both even-parity and odd-parity magnetic fluctuations was studied by means of field line integration, and it was shown that the most-displaced field lines start to decorrelate from the magnetic field at $\beta \approx \beta_{\text{crit}}^{\text{NZT}}$. Furthermore, the SMT-induced resonant B_x components were found to catalyze the NZT effect and reduce the threshold. An analysis of the nonlinear energy transfer associated with zonal flows yields results consistent with these findings: below $\beta_{\text{crit}}^{\text{NZT}}$, zonal flows help saturate the ITG mode whereas this is no longer the case above the threshold, with even net fueling of the overall growth being observed for some k_y.

In conclusion, it was shown in this work that the non-zonal transition is a physical phenomenon showcasing many interesting effects. Further study along these lines would include, in particular, addressing the question whether fusion experiments may be limited operationally by $\beta_{\text{crit}}^{\text{NZT}}$.

ACKNOWLEDGMENTS

The authors wish to express their gratitude to R. E. Waltz, F. I. Parra, and G. W. Hammett for valuable discussions on the subject of this work. We would also like to thank J. Candy and A. G. Peeters for granting permission to use their simulation data in Fig. 1. Some simulations were performed on the Helios system at the International Fusion Energy Research Centre, Aomori, Japan, under the Broader Approach collaboration between Euratom and Japan implemented by Fusion for Energy and JAEA.

[1]M. J. Pueschel, P. W. Terry, F. Jenko, D. R. Hatch, W. M. Nevins, T. Görler, and D. Told, Phys. Rev. Lett. **110**, 155005 (2013).
[2]J. Candy, R. E. Waltz, and M. N. Rosenbluth, Phys. Plasmas **11**, 1879 (2004).
[3]D. R. Hatch, M. J. Pueschel, F. Jenko, W. M. Nevins, P. W. Terry, and H. Doerk, Phys. Rev. Lett. **108**, 235002 (2012).
[4]W. M. Nevins, E. Wang, and J. Candy, Phys. Rev. Lett. **106**, 065003 (2011).
[5]A. J. Brizard and T. S. Hahm, Rev. Mod. Phys. **79**, 421 (2007).
[6]F. Jenko, W. Dorland, M. Kotschenreuther, and B. N. Rogers, Phys. Plasmas **7**, 1904 (2000).
[7]See http://gene.rzg.mpg.de for code details and access.
[8]W. M. Nevins, J. Candy, S. Cowley, T. Dannert, A. Dimits, W. Dorland, C. Estrada-Mila, G. W. Hammett, F. Jenko, M. J. Pueschel, and D. E. Shumaker, Phys. Plasmas **13**, 122306 (2006).
[9]G. L. Falchetto, B. D. Scott, P. Angelino, A. Bottino, T. Dannert, V. Grandgirard, S. Janhunen, F. Jenko, S. Jolliet, A. Kendl, B. F. McMillan, V. Naulin, A. H. Nielsen, M. Ottaviani, A. G. Peeters, M. J. Pueschel, D. Reiser, T. T. Ribeiro, and M. Romanelli, Plasma Phys. Controlled Fusion **50**, 124015 (2008).
[10]X. Lapillonne, B. F. McMillan, T. Görler, S. Brunner, T. Dannert, F. Jenko, F. Merz, and L. Villard, Phys. Plasmas **17**, 112321 (2010).
[11]M. J. Pueschel, F. Jenko, D. Told, and J. Büchner, Phys. Plasmas **18**, 112102 (2011).
[12]M. J. Pueschel, M. Kammerer, and F. Jenko, Phys. Plasmas **15**, 102310 (2008).
[13]A. M. Dimits, G. Bateman, M. A. Beer, B. I. Cohen, W. Dorland, G. W. Hammett, C. Kim, J. E. Kinsey, M. Kotschenreuther, A. H. Kritz, L. L. Lao, J. Mandrekas, W. M. Nevins, S. E. Parker, A. J. Redd, D. E. Shumaker, R. Sydora, and J. Weiland, Phys. Plasmas **7**, 969 (2000).

[14]J. Candy, Phys. Plasmas **12**, 72307 (2005).
[15]A. Arakawa, J. Comp. Phys. **1**, 119 (1966).
[16]M. J. Pueschel, T. Dannert, and F. Jenko, Comput. Phys. Commun. **181**, 1428 (2010).
[17]R. E. Waltz, Phys. Plasmas **17**, 072501 (2010).
[18]W. M. Nevins, E. Wang, I. Joseph, J. Candy, S. E. Parker, Y. Chen, and G. Rewoldt, "Turbulence-driven magnetic reconnection," in *51st Annual Meeting of the APS Division of Plasma Physics* (American Physical Society, 2009).
[19]J. Candy and R. E. Waltz, J. Comput. Phys. **186**, 545 (2003).
[20]A. G. Peeters, Y. Camenen, F. J. Casson, W. A. Hornsby, A. P. Snodin, D. Strintzi, and G. Szepesi, Comput. Phys. Commun. **180**, 2650 (2009).
[21]M. J. Pueschel and F. Jenko, Phys. Plasmas **17**, 062307 (2010).
[22]M. N. Rosenbluth and F. L. Hinton, Phys. Rev. Lett. **80**, 724 (1998).
[23]F. L. Hinton and M. N. Rosenbluth, Plasma Phys. Controlled Fusion **41**, A653 (1999).
[24]M. J. Pueschel, T. Görler, F. Jenko, D. R. Hatch, and A. J. Cianciara, "On secondary and tertiary instability in electromagnetic plasma micro-turbulence," Phys. Plasmas (submitted).
[25]H. Sugama and T.-H. Watanabe, Phys. Plasmas **13**, 012501 (2006).
[26]M. J. Pueschel, Ph.D. thesis, University of Münster, 2009.
[27]J. Connor, R. Hastie, and J. Taylor, Phys. Rev. Lett. **40**, 396 (1978).
[28]E. Wang, W. M. Nevins, J. Candy, D. Hatch, P. Terry, and W. Guttenfelder, Phys. Plasmas **18**, 056111 (2011).
[29]H. Doerk, F. Jenko, M. J. Pueschel, and D. R. Hatch, Phys. Rev. Lett. **106**, 155003 (2011).
[30]D. R. Hatch, P. W. Terry, F. Jenko, F. Merz, M. J. Pueschel, W. M. Nevins, and E. Wang, Phys. Plasmas **18**, 055706 (2011).
[31]H. Doerk, F. Jenko, T. Görler, D. Told, M. J. Pueschel, and D. R. Hatch, Phys. Plasmas **19**, 055907 (2012).
[32]D. R. Hatch, M. J. Pueschel, F. Jenko, W. M. Nevins, P. W. Terry, and H. Doerk, Phys. Plasmas **20**, 012307 (2013).
[33]M. J. Pueschel, F. Jenko, M. Schneller, T. Hauff, S. Günter, and G. Tardini, Nucl. Fusion **52**, 103018 (2012).
[34]R. E. Waltz and G. M. Staebler, Phys. Plasmas **15**, 014505 (2008).
[35]C. Holland, P. H. Diamond, S. Champeaux, E. Kim, O. Gurcan, M. N. Rosenbluth, G. R. Tynan, N. Crocker, W. Nevins, and J. Candy, Nucl. Fusion **43**, 761 (2003).
[36]M. Nakata, T.-H. Watanabe, and H. Sugama, Phys. Plasmas **19**, 022303 (2012).
[37]A. B. Navarro, P. Morel, M. Albrecht-Marc, D. Carati, F. Merz, T. Görler, and F. Jenko, Phys. Plasmas **18**, 092303 (2011).
[38]A. B. Navarro, P. Morel, M. Albrecht-Marc, D. Carati, F. Merz, T. Görler, and F. Jenko, Phys. Rev. Lett. **106**, 055001 (2011).
[39]G. G. Plunk, T. Tatsuno, and W. Dorland, New J. Phys. **14**, 103030 (2012).
[40]P. H. Diamond, S.-I. Itoh, K. Itoh, and T. S. Hahm, Plasma Phys. Controlled Fusion **47**, R35 (2005).